metals

MDPI

Article

Ni-Fe Alloy Coatings Prepared via Jet Electrodeposition for the Optimization of the Electrochemical Detection Performance of Laser-Induced Graphene for Pb(II)

Jiaming Gao [1], Haiwei Fu [1], Chen Liu [2], Yifan Zhu [1,*] and Xiuqing Fu [1,*]

[1] College of Engineering, Nanjing Agricultural University, Nanjing 210031, China; 9203011705@stu.njau.edu.cn (J.G.); 9193011804@stu.njau.edu.cn (H.F.)
[2] China National Heavy Duty Truck Group, Jinan 250031, China; 13064059645@163.com
* Correspondence: yifan.zhu@njau.edu.cn (Y.Z.); fuxiuqing@njau.edu.cn (X.F.); Tel.: +86-187-5188-4081 (Y.Z.); +86-139-1387-8179 (X.F.)

Abstract: Heavy metal pollution in water, particularly Pb ion pollution, has seriously threatened human life and health. Therefore, the manufacture of efficient and sensitive heavy metal ion detection materials is essential. The objective of this study was to improve the electrochemical detection performance of laser-induced graphene (LIG) for Pb(II). Considering the excellent ion affinity and high activity of transition metals, Ni-Fe alloy coatings were prepared on the surface of LIG through jet electrodeposition. The prepared LIG and Ni-Fe/LIG were qualitatively analyzed through Raman spectrometry, X-ray diffraction analysis, scanning electron microscopy, and energy-dispersive X-ray spectroscopy. The surface micromorphologies, charge transfer capabilities, and electrochemically active surface areas of LIG and Ni-Fe/LIG were characterized. The detection range and limit of detection (LOD) of Pb(II) for LIG and Ni-Fe /LIG as electrochemical sensors were analyzed. Results showed that compared with LIG, Ni-Fe/LIG had more surface active sites, a higher charge transfer capability, and a larger electrochemically active surface area that reached 0.828 cm^2. Ni-Fe/LIG had a detection range of 20–1200 μg/L and an LOD of as low as 0.771 μg/L. Ni-Fe/LIG demonstrated a better electrochemical detection performance for Pb(II) than LIG when used as an electrochemical sensor.

Keywords: Pb(II) detection; Ni-Fe/LIG; jet electrodeposition; electrochemical sensor

check for updates

Citation: Gao, J.; Fu, H.; Liu, C.; Zhu, Y.; Fu, X. Ni-Fe Alloy Coatings Prepared via Jet Electrodeposition for the Optimization of the Electrochemical Detection Performance of Laser-Induced Graphene for Pb(II). *Metals* **2023**, *13*, 1253. https://doi.org/10.3390/met13071253

Academic Editor: Henrik K Hansen

Received: 23 May 2023
Revised: 30 June 2023
Accepted: 6 July 2023
Published: 9 July 2023

Copyright: © 2023 by the authors. Licensee MDPI, Basel, Switzerland. This article is an open access article distributed under the terms and conditions of the Creative Commons Attribution (CC BY) license (https://creativecommons.org/licenses/by/4.0/).

1. Introduction

With the rapid development of modern industries, the problem of heavy metal pollution in water has become increasingly serious [1]. Heavy metal pollutants, such as Pb(II), exist in water for a long time, are difficult to degrade, and seriously harm the environment [2]. An excessive intake of Pb(II) will be harmful to most human systems, causing diseases, such as hypertension, stomach illnesses, and kidney failure. In severe cases, Pb(II) intake can be fatal [3]. Therefore, achieving an accurate and efficient detection of heavy metal ions in water, particularly Pb ions, is highly necessary.

At present, common heavy metal ion detection methods can be classified into spectroscopic [4], biological [5], and electrochemical methods [6]. The electrochemical method, especially anodic stripping voltammetry, has broad application prospects in the field of heavy metal detection because of its low cost and strong anti-interference ability [7]. A commonly used electrochemical detection system is a three-electrode system, which includes a working electrode (WE), a reference electrode (RE), and a counter electrode (CE) [8]. The WE, which acts as the electrochemical sensor, determines detection ability. Sensor materials should exhibit good adsorption. Many active sites and a large electrochemical active surface area can improve the accuracy and efficiency of detection to a certain extent.

Commonly used sensor materials include metal materials, metal oxides, carbon materials, and biological materials [9,10]. Graphene exhibits the advantages of a large surface area and a high charge transfer capability because of its unique crystal structure [11–13]. Therefore, graphene is widely used in microelectronics, energy storage, sensors, and other fields [14,15].

However, traditional graphene preparation methods, such as mechanical exfoliation, chemical vapor deposition, and redox methods [16–18], have disadvantages, including a complex process, high cost, and low efficiency. These disadvantages considerably limit the further application of graphene.

In 2014, Tour et al. successfully generated laser-induced graphene (LIG) on polyimide (PI) film substrate by using a CO_2 infrared laser in an atmospheric environment [19]. This method is simple, economical, and efficient and it generates LIG with an extremely large surface area and high charge transfer capability [19,20]. Therefore, LIG is an ideal electrode material for electrochemical detection. LIG has been used in the directional detection of sweat [21], dopamine [22], and glucose [23] in the human body and heavy metal ions such as Zn, Pd, and Cd [24], in water.

In recent years, many scholars have successfully conducted research on the surface modification of LIG to improve its electrochemical detection performance as an electrochemical sensor and increase its detection range and limit of detection (LOD). Given the excellent ionic affinity and high activity of transition metals, the electrochemical detection performance of LIG can be enhanced by depositing Ni and Fe metal particles onto its surface. Huang et al. prepared Ni-Fe/LIG composite structures and found that distributing Ni-Fe nanoparticles on the surface of LIG could increase the surface active sites of Ni-Fe/LIG [25]. Zhang et al. demonstrated that Ni-Fe/LIG had a high electrochemically active surface area and excellent charge transfer capability [26]. Existing methods for preparing Ni-Fe alloy on LIG surfaces are mostly based on laser etching. The prepared Ni-Fe/LIG has some defects, such as the uneven and insufficient distribution of Ni and Fe elements. Moreover, the internal physical and chemical properties of Ni-Fe/LIG differ.

Electrochemical deposition is a common method for the surface modification of electrode materials. Jet electrodeposition demonstrates the advantages of locality, high efficiency, good performance, easy control, and low cost [27–29]. It can accelerate the ion deposition rate, refine the grain structure of coatings, and improve the surface performance of coatings, and thus, it is suitable for the preparation of alloy coatings [30–32]. On the basis of these advantages, LIG was produced in the current work through laser etching with PI film as the substrate. Ni-Fe alloy coatings were prepared on the surface of LIG through jet electrodeposition to investigate the effects of Ni-Fe alloy coatings on the surface micromorphology, charge transfer capability, and electrochemically active surface area of LIG. Simultaneously, the detection range and LOD of Pb(II) by LIG and Ni-Fe/LIG as electrochemical sensors were analyzed and compared through electrochemical experiments.

2. Materials and Methods

2.1. Materials

PI film (100%) was purchased from Shenzhen Lexin Plastic Industry Co., Ltd. (Shenzhen, China). Polydimethylsiloxane (PDMS, 100%) was purchased from Smooth-on, Inc. (Macugie, PA, USA). Thiourea (CH_4N_2S) and sodium dodecyl sulfate ($C_{12}H_{25}SO_4Na$) were purchased from Shanghai Macklin Biochemical Co., Ltd. (Shanghai, China). Nickel sulfate hexahydrate ($NiSO_4{\cdot}6H_2O$), ferrous sulfate heptahydrate ($FeSO_4{\cdot}7H_2O$), citric acid ($C_6H_8O_7$), boric acid (H_3BO_3), potassium ferricyanide ($K_3[Fe(CN)_6]$), potassium chloride (KCl), sodium acetate (CH_3COONa), glacial acetic acid (CH_3COOH), and Pb(II) standard solution (1000 μg/mL) were purchased from Shanghai Aladdin Biochemical Technology Co., Ltd. (Shanghai, China).

A total of 2.051 g of sodium acetate was dissolved in a beaker, mixed with 2 mL of glacial acetic acid in a 250 mL volumetric flask stirred, mixed, and brought to volume to prepare 0.1 mol/L NaAc HAC buffer solution (pH = 5). All the chemicals were used as received without further purification. All solutions were prepared with deionized water (DIW).

2.2. Experiments

PI film with the thickness of 100 µm was ultrasonically cleaned, vacuum dried, and cut into a rectangle with the dimensions of 5 cm × 7 cm. The film was adhered onto a 5 cm × 8 cm glass sheet with PDMS and heated on a heating table at 80 °C for 3 min to solidify the PDMS and ensure that the PI film was tightly connected to the glass sheet. The preparation of the substrate was thus completed. The prepared substrate was fixed onto the platform of the laser engraving machine then subjected to laser etching under the conditions of the focal length of 13 mm, laser power of 10.0%, and scanning speed of 25 mm/s. The initial LIG was obtained on the surface of PI film after laser etching. It was separated from the glass sheet and trimmed into a suitable size with scissors. The preparation of LIG was thus completed. The whole preparation process is shown in Figure 1.

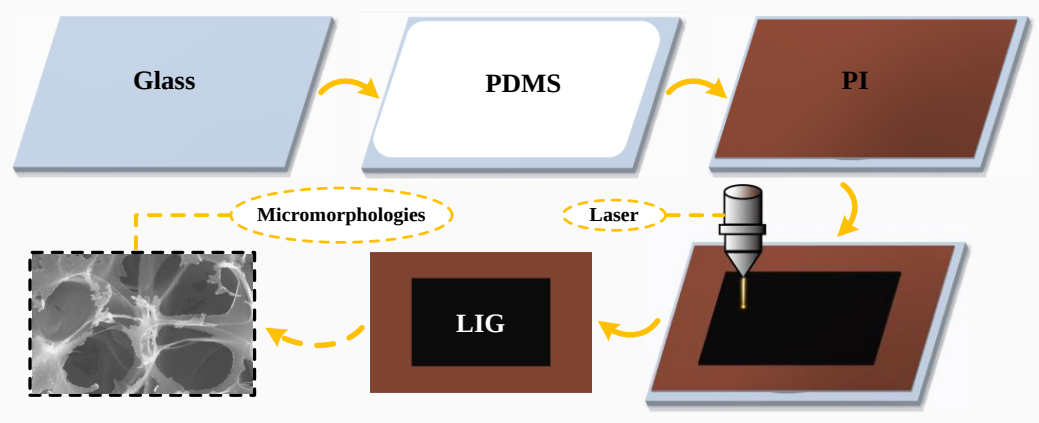


Figure 1. LIG preparation.

The jet electrodeposition equipment was set up as shown in Figure 2. The composition of plating solution is provided in Table 1 [29]. A nozzle with a nickel rod was installed on the spindle of the machine tool. The prepared LIG was adhered onto the clamping device with conductive double-sided adhesive tape, and the clamping device was fixed on the installation platform. The nickel rod was connected to the positive pole of the power supply, and the clamping device was connected to the negative pole of the power supply. Jet electrodeposition was carried out in accordance with the test parameters presented in Table 2. During the processing, the anode nozzle sprayed plating solution onto the cathode LIG to form a closed loop. Under the action of an electric field, Ni(II) and Fe(II) underwent reduction on the surface of LIG, and the Ni-Fe alloy coatings were deposited. After processing, the prepared Ni-Fe/LIG was removed from the platform and washed with DIW. The preparation of Ni-Fe/LIG was thus completed.

Table 1. Composition of the plating solution.

Composition	Content/($g \cdot L^{-1}$)	Effect
$NiSO_4 \cdot 6H_2O$	180	Provide Ni^{2+}
$FeSO_4 \cdot 7H_2O$	30	Provide Fe^{2+}
$C_6H_8O_7$	30	Complexing agent
H_3BO_3	30	pH SRP
CH_4N_2S	0.01	Stabilizer
$C_{12}H_{25}SO_4Na$	0.08	Surfactant

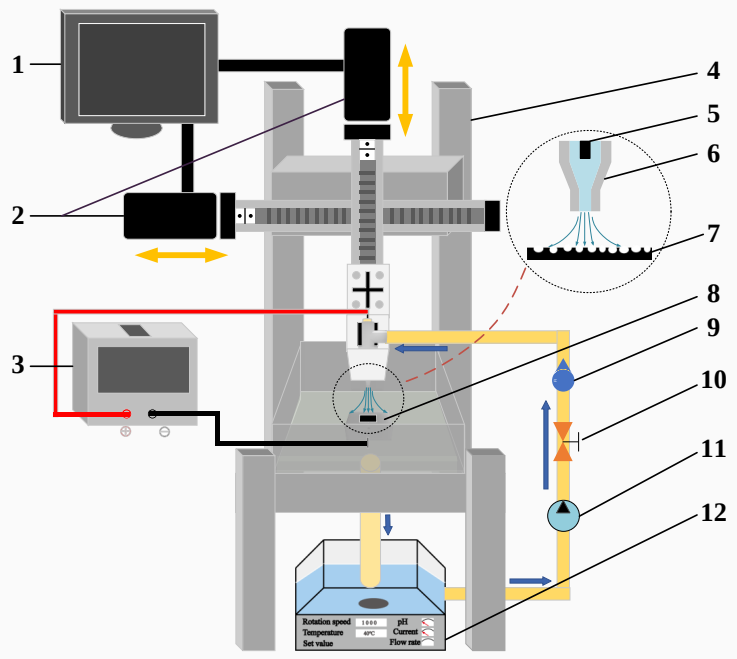


Figure 2. Jet electrodeposition equipment; 1—numerical control system; 2—motor system; 3—power supply; 4—aluminum profile support; 5—nickel rod; 6—nozzle; 7—LIG; 8—clamping device; 9—flowmeter; 10—valve; 11—pump; 12—thermostat water bath.

Table 2. Test parameters of jet electrodeposition.

Parameters	Numerical Value
Current	0.02 A
Temperature	40 °C
Machining gap	1.5 mm
Processing time	10 min
Scanning length	−15–15 mm
pH	3.5–4.0

2.3. Instruments

LIG was qualitatively analyzed through the following methods: a HR800 Raman spectrometer (Raman) from Hitachi, Inc. (Tokyo, Japan) was applied to examine the structural characteristics of graphene in LIG. An X-ray diffractometer (XRD) from PANalytical, Inc. (Almelo, The Netherlands) was used to analyze the phase structure of LIG. A Quanta FEG 250 field-emission scanning electron microscope (SEM) from FEI Instruments, Inc. (Hillsboro, OR, USA) was utilized to investigate the surface and cross-sectional micromorphologies of LIG. Ni-Fe/LIG was qualitatively analyzed through the following methods: an energy dispersive spectroscope (EDS) from Bruker AXS, Inc. (Berlin, Germany) was employed to investigate the elements of Ni-Fe/LIG; XRD was used to analyze the phase structure of Ni-Fe/LIG.

SEM was utilized to compare the surface micromorphologies of LIG and Ni-Fe/LIG. At the same time, an electrochemical workstation (CS350, Wuhan CorrTest Instruments Corp. Ltd., Wuhan, China) was used to perform electrochemical experiments through a three-electrode-cell electrochemical test method. The working electrode was LIG or Ni-Fe/LIG, the auxiliary electrode was Pt, and the reference electrode was a saturated calomel electrode. The charge transfer capabilities of LIG and Ni-Fe/LIG were compared through cyclic voltammetry (CV) in 5 mmol/L $K_3[Fe(CN)]_6$ solution [33] containing 1 mol/L KCl over the scanning voltage range of +0.5 V to −0.2 V at the scanning rate of 130 mV/s. Then, for the calculation of the electrochemically active surface areas of LIG and Ni-Fe/LIG, the

scanning voltage range was kept constant and the scanning rate was varied from 10 mV/s to 130 mV/s to obtain the CV curves of LIG and Ni-Fe/LIG at different scanning rates.

By using a CS350 electrochemical workstation, LIG and Ni-Fe/LIG were successively used as electrochemical sensors for the electrochemical detection experiments at different Pb(II) concentrations through square-wave pulse anodic stripping voltammetry (SWASV) in 0.1 mol/L NaAc-HAc buffer solution (pH = 5) [34]. Pb(II) solutions with different concentrations were prepared from 1000 μg/mL Pb(II) standard solution. In this experiment, the LIG and Ni-Fe/LIG electrodes were successively immersed into the mixed liquor containing 0.1 mol/L NaAc-HAc buffer solution and the Pb(II) solution. The enrichment potential was −1 V, and the enrichment time was 200 s [35]. The Pb(II) in the solution were reduced into Pb and enriched in the electrode surface. Then, stripping was performed. All the stripping processes were carried out under the following experimental conditions: an amplitude of 25 mV, an increment potential of 4 mV, and a frequency of 15 Hz [33,35,36]. The SWASV curves at different Pb(II) concentrations were obtained through their corresponding stripping processes. The peak current of SWASV curves at different Pb(II) concentrations and the corresponding Pb(II) concentration values were analyzed linearly to obtain the standard curves of LIG and Ni-Fe/LIG for the detection of Pb(II) concentrations.

3. Results and Discussion

3.1. Qualitative Analysis of LIG and Ni-Fe/LIG

3.1.1. Qualitative Analysis of LIG

Figure 3 shows the physical characterization of LIG produced by laser etching on PI film. Figure 3a presents the principle of laser-induced graphene. When the laser is irradiated onto PI film, the local surface temperature rapidly increases, which causes etching by photothermal effect. The N–C with the lowest binding force in the PI film is the first to be broken and separated. Meanwhile, separated elements combine with each other or other elements in the atmosphere to form various forms of compounds, such as CO, CN, CH, C_2H_2, HCN [37].

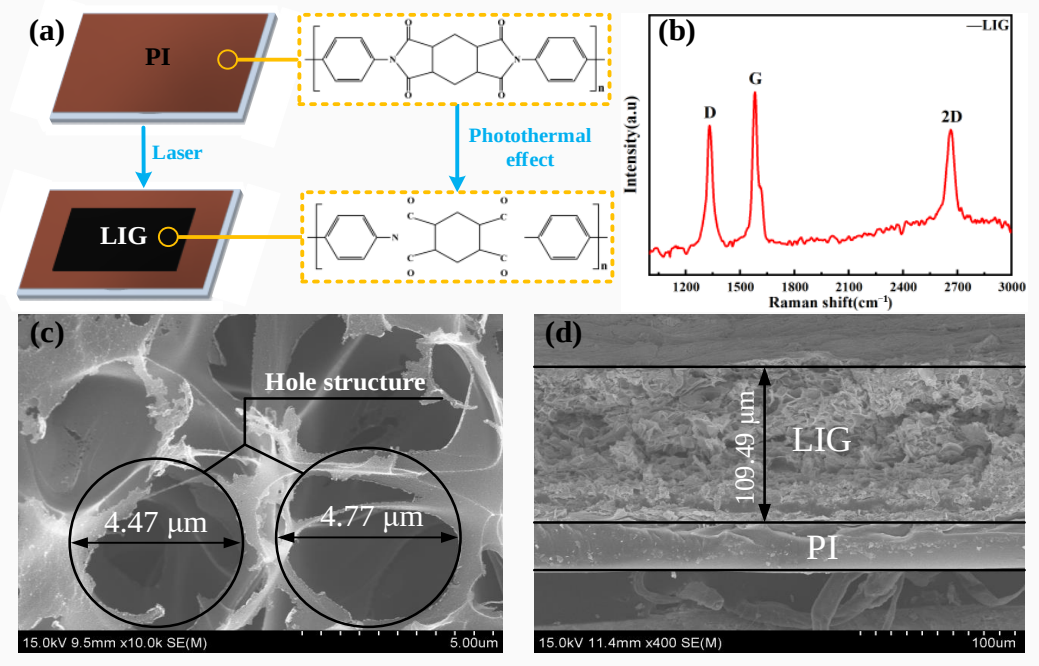


Figure 3. Physical characterization analysis of LIG: (**a**) Principle of preparing LIG; (**b**) Raman scatteringspectrum of LIG; (**c**) SEM surface micromorphology of LIG; (**d**) SEM cross-sectional micromorphology of LIG.

Figure 3b presents the Raman scattering spectrum of the generated LIG. The figure shows the presence of obvious characteristic bands at 1332, 1583, and 2665 cm^{-1} that corresponded to the D, G, and 2D bands of the LIG standard spectrum, respectively, indicating that the substance is indeed LIG. The D-band represents the disordered structure and defect degree of graphene, the G-band represents the in-plane vibration of the sp^2-carbon atom, and the 2D-band represents the interlayer stacking mode of C atoms [38,39]. The Raman spectrum indicates that a multilayered graphene structure has been successfully formed by laser etching technology [40,41].

Figure 3c,d presents the surface and cross-sectional micromorphologies of LIG under SEM. Figure 3c illustrates that the LIG produced on PI film through laser etching presents a complex irregular three-dimensional porous network structure because during laser etching on PI film, the photothermal effect of the laser causes the PI film to decompose at high temperatures after carbonization, and the original C–O, C=O, and N–C break, recombine, and escape in the form of gas [19], thus resulting in the formation of hole-like structures. At the same time, the time to form the standard hexagonal graphene structure is insufficient due to the rapid cooling rate after laser etching, and the inside of LIG presents an irregular three-dimensional porous network structure. Figure 3d shows that the LIG that has formed above the PI film has copious holes, and its thickness is 109.49 μm; these internal structures increase the surface area of LIG.

3.1.2. Qualitative Analysis of Ni-Fe/LIG

Figure 4a shows the XRD characterization results of Ni-Fe/LIG. In this figure, the diffraction peaks at $2\theta = 44.6°$ correspond to the characteristic peak of Ni-Fe (110), indicating that Ni-Fe alloy coatings have been successfully prepared on the LIG surface and that Ni-Fe/LIG has been formed successfully.

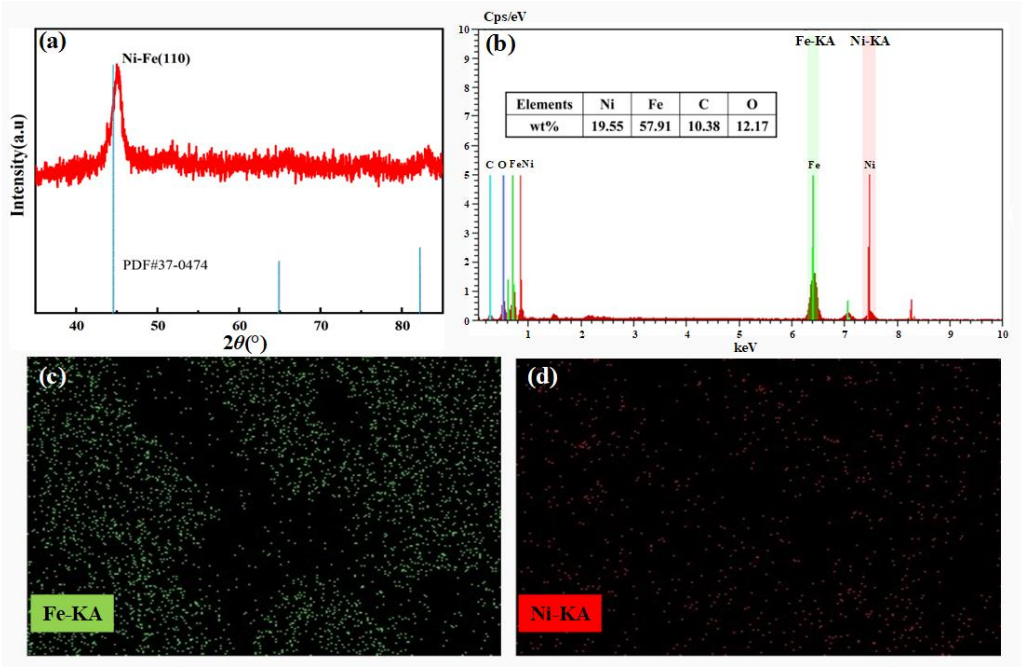


Figure 4. XRD and EDS patterns of Ni-Fe/LIG: (**a**) XRD pattern of Ni-Fe/LIG; (**b**) graph of the characteristic peaks of Ni-Fe/LIG; (**c**) EDS element distribution of Fe; (**d**) EDS element distribution of Ni.

Figure 4b–d present the EDS characterization results of Ni-Fe/LIG. Figure 4b is a graph of the characteristic peaks of each element. The graph clearly shows the four characteristic peaks representing the C, O, Fe, and Ni elements, and the relative contents of Ni and Fe are 19.55 wt% and 57.91 wt%. This result indicates that Ni and Fe elements have been deposited on the surface of LIG and that Ni-Fe/LIG has been successfully prepared. Figure 4c,d show the distribution of Fe and Ni elements. Ni and Fe elements are uniformly distributed on the

surface of LIG, and Ni-Fe alloy coatings prepared through jet electrodeposition are even and effective.

3.2. Analysis of the Surface Micromorphology of LIG and Ni-Fe/LIG

Figure 5a,b show the SEM surface micromorphology of LIG. The surface of LIG prepared through laser etching has a three-dimensional porous network structure with numerous holes and a large surface area, which provides a large number of attachment sites for the deposition of Ni and Fe elements [42], and the average pore size of LIG is 5.06 μm.

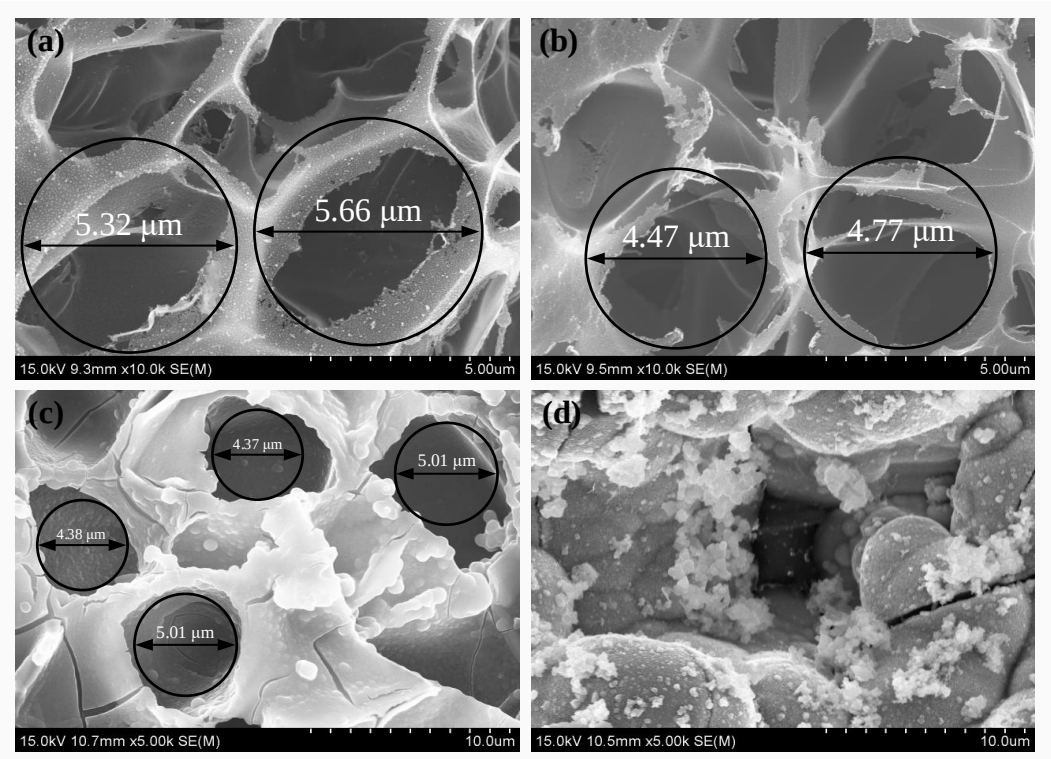


Figure 5. SEM surface micromorphology of LIG and Ni-Fe/LIG: (**a**,**b**) SEM surface micromorphology of LIG; (**c**) SEM surface micromorphology of Ni-Fe/LIG; (**d**) SEM hole micromorphology of Ni-Fe/LIG.

Figure 5c,d depict the SEM surface and hole micromorphologies of Ni-Fe/LIG. As shown in Figure 5c, the Ni-Fe alloy coatings do not change the original three-dimensional porous internal structure of LIG, and high numbers of microspherical structures representing the Ni-Fe alloy coatings are widely deposited on the hole surfaces and walls of LIG. As nickel and iron are transition metal elements, they have good electrocatalysis and conductivity, which are conducive to charge transfer on the Ni-Fe/LIG electrode and the acceleration of oxidation and reduction [43]. Therefore, combined with image information, this result shows that the Ni-Fe alloy coatings improve the surface active sites of LIG, and a multitude of microspherical structures representing the Ni-Fe alloy coatings provide Ni-Fe/LIG with more surface active sites than LIG. At the same time, the pore size of Ni-Fe/LIG is smaller than that of LIG due to the deposition of Ni-Fe alloy coatings, and its average value is 4.69 μm.

Figure 5d illustrates that the microspherical structures representing the Ni-Fe alloy coatings have completely covered the internal hole wall surfaces of LIG. This effect greatly increases the surface active sites of Ni-Fe/LIG.

Therefore, Ni-Fe/LIG has more surface active sites than LIG. This characteristic is beneficial for improving the detection range of Ni-Fe/LIG as an electrochemical sensor.

3.3. Analysis of the Charge Transfer Capabilities and Electrochemically Active Surface Areas of Lig and Ni-Fe/Lig

The detection efficiency of an electrochemical sensor depends on charge transfer capability to some extent. Figure 6a,b, respectively, present the CV curves of LIG and Ni-Fe/LIG in 5 mmol/L $K_3[Fe(CN)_6]$ solution containing 1 mol/L KCl solution acquired over the scanning voltage range of +0.5 V to −0.2 V at the scanning rate of 130 mV/s.

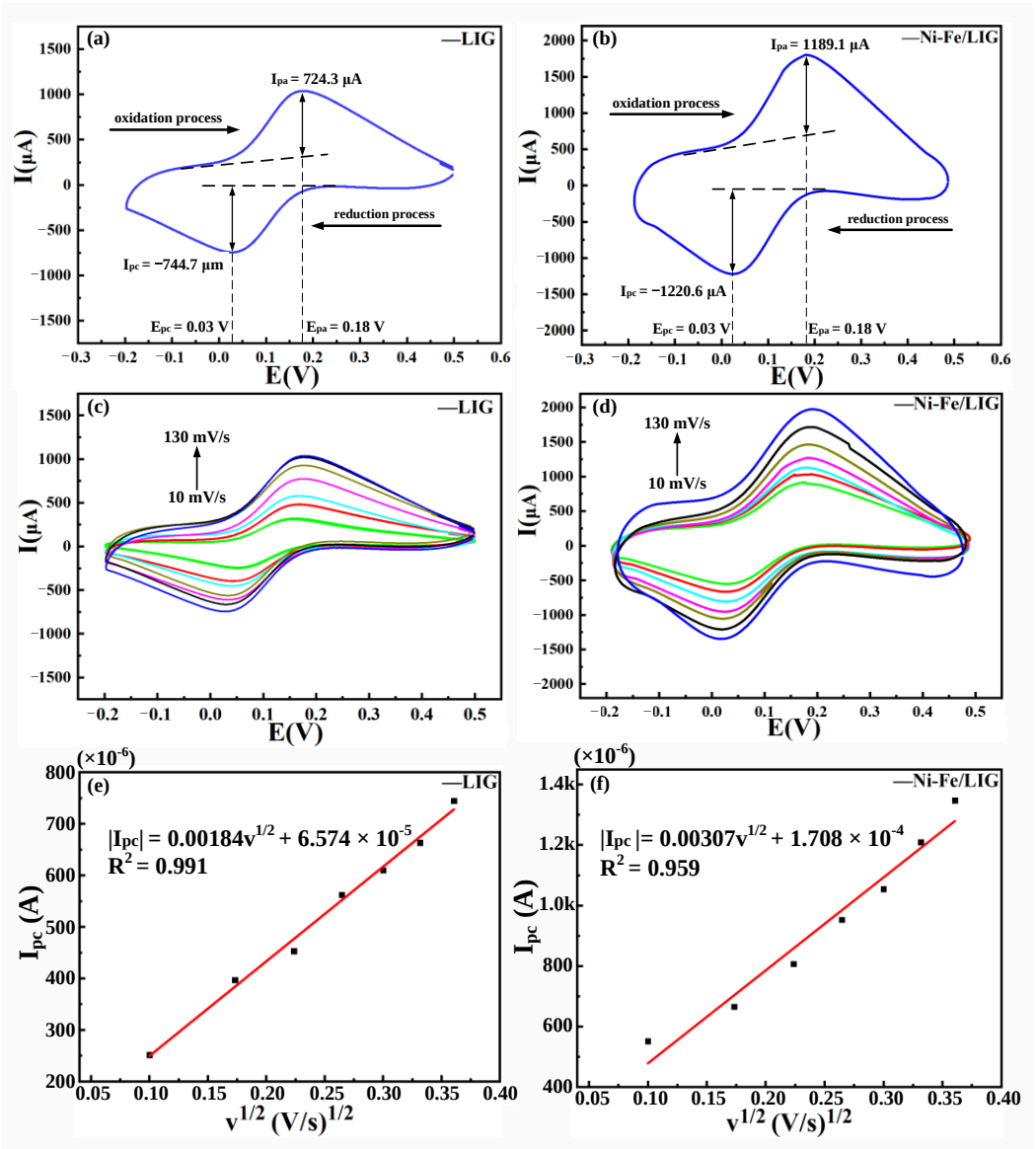


Figure 6. CV curve analysis diagram of LIG and Ni-Fe/LIG: (**a**) CV curve of LIG at the scanning rate of 130 mV/s; (**b**) CV curve of Ni-Fe/LIG at the scanning rate of 130 mV/s; (**c**) CV curves of LIG at different scanning rates (10–130 mV/s); (**d**) CV curves of Ni-Fe/LIG at different scanning rates (10–130 mV/s); (**e**) linear relation curve of the I_{pc} and $v^{1/2}$ of LIG; (**f**) linear relation curve of the I_{pc} and $v^{1/2}$ of Ni-Fe/LIG.

Figure 6a,b show that LIG and Ni-Fe/LIG have the same anodic peak potential of E_{pa} = 0.18 V and the same cathodic peak potential of E_{pc} = 0.03 V. LIG has the anodic peak current of I_{pa} = 724.3 μA and the cathodic peak current of $|I_{pc}|$ = 744.7 μA. Ni-Fe/LIG has the anodic peak current of I_{pa} = 1189.1 μA > 724.3 μA and the cathodic peak current of $|I_{pc}|$ = 1220.6 μA > 744.7 μA. These results indicate that the charge transfer capability of Ni-Fe/LIG is better than that of LIG. Oxidation and reduction on the Ni-Fe/LIG electrode are faster than those on the LIG electrode, and the charge transfer rate is high. Ni and

Fe elements are transition metals and thus have good conductivity and catalytic activity, which are conducive to charge transfer on the Ni-Fe/LIG electrode and the acceleration of oxidation and reduction [43]. At the same time, the Ni-Fe alloy coatings increase the surface active sites of LIG. This effect is conducive to the contact between the electrolyte and the surface active sites of Ni-Fe/LIG and ensures an effective charge transfer between electrode and electrolyte. Given that the detection efficiency of the electrochemical sensor depends on its charge transfer capability, that is, the speed of oxidation and reduction on the surface of the working electrode, Ni-Fe/LIG has a higher detection efficiency than LIG when used as an electrochemical sensor [26].

The influence of scanning rate (v) on peak current (I_{pc}) was analyzed as depicted in Figure 6c–f to calculate the electrochemically active surface areas of LIG and Ni-Fe/LIG. Figure 6c,d show, respectively, the set of the CV curves of LIG and Ni-Fe/LIG obtained at the different scanning rates of 10, 30, 50, 70, 90, 110, and 130 mV/s. The relationship between the I_{pc} and v of LIG and Ni-Fe/LIG is presented in Figure 6e,f. The figure shows that the I_{pc} of LIG and Ni-Fe/LIG is linearly related to $v^{1/2}$. This relationship indicates that the reduction process in the CV curve of LIG and Ni-Fe/LIG is a diffusion control process. Thus, the Randles-Sevcik equation can be used to calculate the electrochemically active surface areas of LIG and Ni-Fe/LIG:

$$I_p = 2.69 \times 10^5 n^{3/2} D^{1/2} A C v^{1/2} = K v^{1/2} \quad (1)$$

where I_p represents the peak current of the CV curve (A), D represents the diffusion coefficient of $K_3[Fe(CN)_6]$ ($D = 7.6 \times 10^{-6}$ cm^2/s), C represents the initial concentration of $K_3[Fe(CN)_6]$ ($C = 5 \times 10^{-6}$ mol/cm^3), n represents the electron transfer number (n = 1), v represents the scanning rate (V/s), and A represents the electrochemically active surface area.

Figure 6e,f are expressed by Formula (1). The linear equations of LIG and Ni-Fe/LIG are as follows:

$$\text{LIG: } |I_{pc}| = 0.00184 v^{1/2} + 6.574 \times 10^{-5} \ (R^2 = 0.991)$$

$$\text{Ni-Fe/LIG: } |I_{pc}| = 0.00307 v^{1/2} + 1.708 \times 10^{-4} \ (R^2 = 0.959)$$

The calculations show that the electrochemically active surface area of LIG is 0.496 cm^2 and that of Ni-Fe/LIG is 0.828 cm^2. Given that 0.828 cm^2 > 0.496 cm^2, Ni-Fe/LIG is proven to have a larger electrochemically active surface area than LIG. A large electrochemically active surface area is beneficial for optimizing the detection performance of Ni-Fe/LIG as an electrochemical sensor.

3.4. Analysis of the Detection Ranges and LOD of Pb (II) by LIG and Ni-Fe /LIG

3.4.1. Analysis of the Detection Range and LOD of Pb(II) by LIG

The detection range and LOD are important parameters for quantifying the performance of an electrochemical sensor. A sensor with a wide detection range and small LOD has high applicability and sensitivity and superior electrochemical detection performance.

Figure 7a presents the SWASV response curves collected when LIG was used as an electrochemical sensor to detect Pb(II) at the concentrations of 20, 30, 40, 50, 60, 70, 80, 90, 100, 200, 300, 400, 500, and 600 μg/L. This figure demonstrates that the peak current (I_p) of the SWASV curve increases with the increase in Pb(II) concentration (C-Pb^{2+}) and that a linear relationship exists between I_p and C-Pb^2. Figure 7c,d show the fitting linear curves of I_p (μA) and C-Pb^{2+} (μg/L) based on the SWASV curve of LIG at the two Pb(II) concentrations of 20–100 and 100–600 μg/L:

$$I_p = 0.108(\text{C-}Pb^{2+}) + 0.529 \ (\text{C-}Pb^{2+}\text{: 20–100 } \mu g/L, R^2 = 0.988)$$

$$I_p = 0.068(\text{C-}Pb^{2+}) + 2.232 \ (\text{C-}Pb^{2+}\text{: 100–600 } \mu g/L, R^2 = 0.969)$$

the LOD of LIG as an electrochemical sensor can be calculated using the following formula:

$$LOD = 3\sigma_b/m \quad (2)$$

where σ_b represents the standard deviation of the blank response, and m represents the slope of the fitting linear curve in the low concentration range [44].

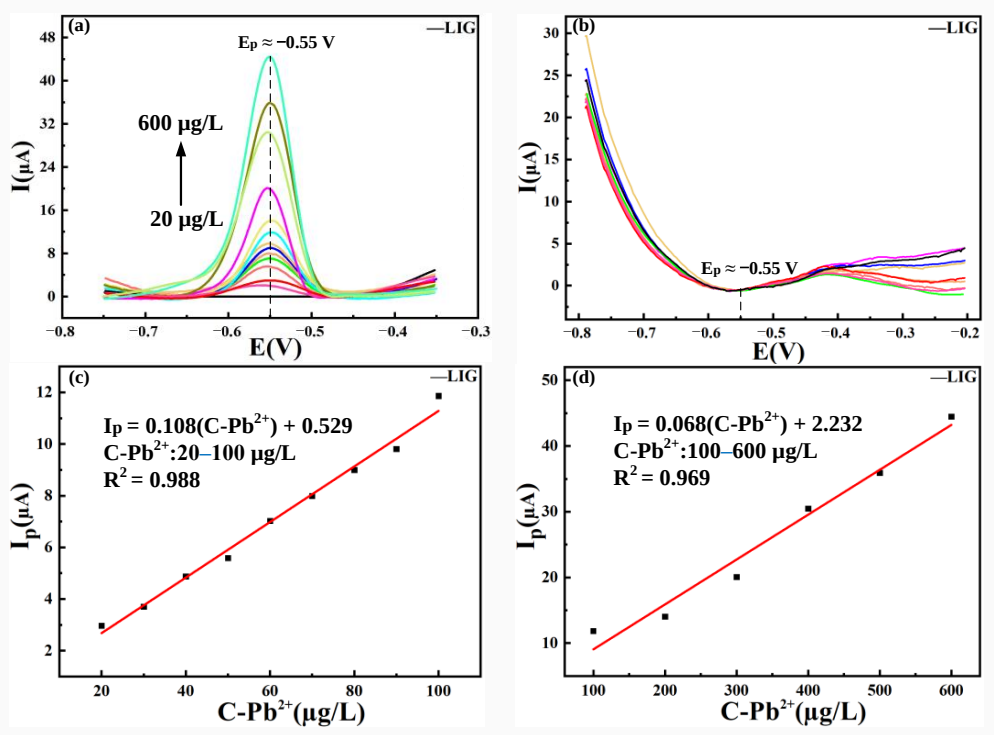


Figure 7. Detection range and LOD analysis of LIG: (**a**) SWASV curves of LIG at different C-Pb^{2+} (20–600 μg/L); (**b**) ten blank response curves of LIG; (**c**) linear relation curve of the I_p of LIG and C-Pb^{2+} (20–100 μg/L); (**d**) linear relation curve of the I_p of LIG and C-Pb^{2+} (100–600 μg/L).

Figure 7b shows the SWASV curves of the 10 blank responses of LIG. The standard deviation was calculated from the current values of the corresponding 10 blank curves when the peak voltage of SWASV curve $E_p = -0.55$ V and is found to be $\sigma_b = 0.0457$. At the same time, given that the slope of the fitting linear curve within the Pb(II) concentrations of 20–100 μg/L is 0.108, m takes the value of 0.108. Therefore, the LOD of LIG calculated by using Formula (2) is 1.269 μg/L, and the detection range of LIG is 20–600 μg/L.

3.4.2. Analysis of the Detection Range and LOD of Pb(II) by Ni-Fe /LIG

Figure 8a shows the SWASV response curves collected when Ni-Fe/LIG was used as an electrochemical sensor to detect Pb(II) at the concentrations of 20, 30, 40, 50, 60, 70, 80, 90, 100, 200, 300, 400, 500, 600, 700, 800, 900, 1000, 1100, and 1200 μg/L.

This figure indicates that the I_p of the SWASV curve also increases with the increase in C-Pb^{2+} and that a linear relationship exists between I_p and C-Pb^{2+}. Figure 8c,d show the fitting linear curves of I_p (μA) and C-Pb^{2+} (μg/L) in the SWASV curve of Ni-Fe/LIG at the two Pb(II) concentrations of 20–100 and 100–1200 μg/L:

$$I_p = 0.193(\text{C-}Pb^{2+}) - 1.064 \ (\text{C-}Pb^{2+}\text{: 20–100 μg/L}, R^2 = 0.984)$$

$$I_p = 0.108(\text{C-}Pb^{2+}) + 0.797 \ (\text{C-}Pb^{2+}\text{: 100–1200 μg/L}, R^2 = 0.988)$$

Figure 8b provides the SWASV curves based on the responses of the 10 Ni-Fe/LIG blanks. The standard deviation was calculated from the current values of the corresponding

10 blank curves when the peak voltage of SWASV curve $E_p = -0.55$ V and is found to be $\sigma_b = 0.0496$. At the same time, given that the slope of the fitting linear curve within the Pb(II) concentrations of 20–100 μg/L is 0.193, m takes the value of 0.193. Thus, the LOD of Ni-Fe/LIG calculated by using Formula (2) is 0.771 μg/L, and the detection range of Ni-Fe/LIG is 20–1200 μg/L.

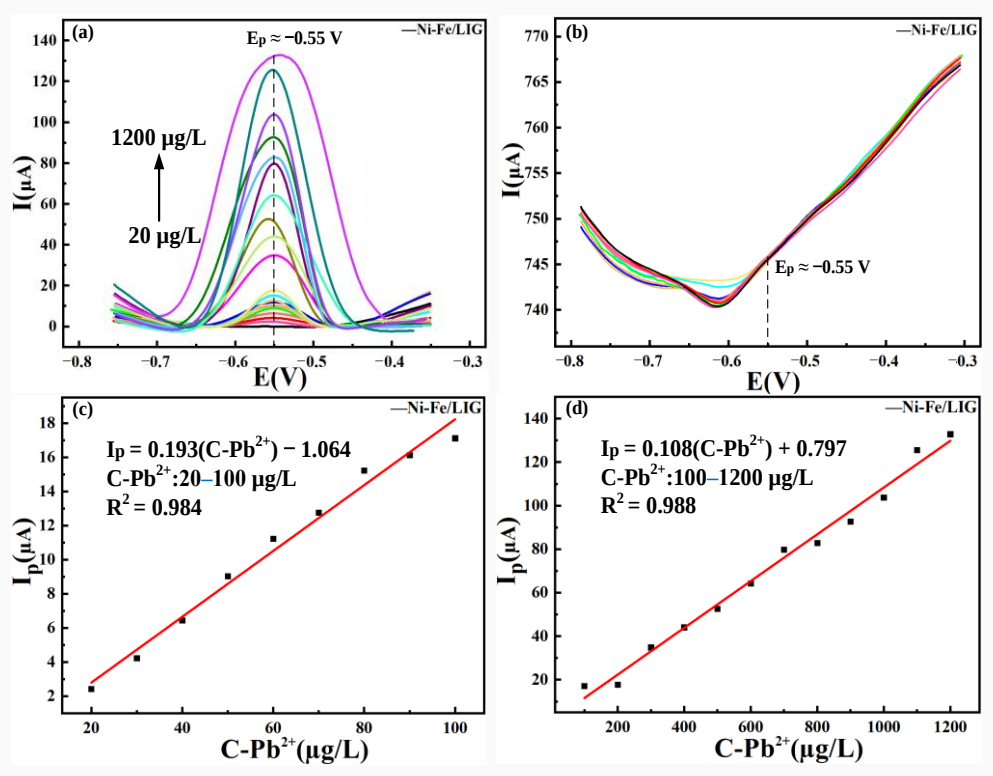


Figure 8. Detection range and LOD analysis of Ni-Fe/LIG: (**a**) SWASV curves of Ni-Fe/LIG at different C-Pb^{2+} (20–1200 μg/L); (**b**) ten blank response curves of Ni-Fe/LIG; (**c**) linear relation curve of the I_p of Ni-Fe/LIG and C-Pb^{2+} (20–100 μg/L); (**d**) linear relation curve of the I_p of Ni-Fe/LIG and C-Pb^{2+} (100–1200 μg/L).

Therefore, when detecting Pb(II), Ni-Fe/LIG has a wider detection range (1200 μg/L > 600 μg/L) and a smaller LOD (0.771 μg/L < 1.269 μg/L) than LIG. As an electrochemical sensor, Ni-Fe/LIG has improved electrochemical detection performance. The Ni-Fe alloy coatings optimize the electrochemical detection performance of LIG successfully. It can detect solutions with low Pb(II) concentrations, and its minimum detectable Pb(II) concentration is 0.771 μg/L.

4. Conclusions

LIG has great application potential in the field of electrochemical detection because of its large surface area and good charge transfer capability. In this study, LIG was generated on PI film via laser etching, and Ni-Fe alloy coatings were prepared on the surfaces of LIG by using jet electrodeposition to further improve the electrochemical detection performance of LIG as an electrochemical sensor. The surface active sites, charge transfer capability, and electrochemically active surface area of LIG and Ni-Fe/LIG were characterized, and the detection range and LOD of LIG and Ni-Fe/LIG as electrochemical sensors were studied through electrochemical experiments. The research results were as follows:

- Ni-Fe/LIG had more surface active sites than LIG. Ni-Fe alloy was fully deposited on the surfaces of LIG's internal hole walls, and the surface active sites increased to retain the original three-dimensional porous network structure of LIG. This effect was beneficial for improving the detection range of Ni-Fe/LIG as an electrochemical sensor.

- Ni-Fe/LIG had a higher charge transfer capability and larger electrochemically active surface area than LIG. The charge transfer capability of Ni-Fe/LIG was higher than that of LIG, and the electrochemically active surface area of Ni-Fe/LIG reached 0.828 cm^2. This characteristic was beneficial for improving the detection efficiency and detection performance of Ni-Fe/LIG as an electrochemical sensor.
- Ni-Fe/LIG had a wider detection range and lower LOD than LIG when used as an electrochemical sensor. Ni-Fe/LIG had the detection range of 20–1200 μg/L and a LOD of as low as 0.771 μg/L. The preparation of Ni-Fe alloy coatings optimized the detection range and LOD of LIG successfully. Therefore, Ni-Fe/LIG had a better electrochemical detection performance than LIG.

Author Contributions: Conceptualization, J.G., H.F. and X.F.; methodology, H.F. and J.G.; software, J.G. and C.L.; validation, X.F., H.F. and C.L.; formal analysis, J.G.; investigation, H.F., J.G. and C.L.; resources, J.G.; data curation, J.G. and C.L.; writing—original draft preparation, H.F. and J.G.; writing—review and editing, H.F., C.L. and Y.Z.; visualization, J.G. and X.F.; supervision, H.F., J.G. and Y.Z.; project administration, Y.Z. and X.F.; funding acquisition, J.G., X.F. and Y.Z. All authors have read and agreed to the published version of the manuscript.

Funding: This research received no external funding.

Data Availability Statement: The data presented in this study are available in the article.

Conflicts of Interest: The authors declare no conflict of interest.

References

1. Zirlianngura; Tiwari, D.; Ha, J.H.; Lee, S.M. Efficient Use of Porous Hybrid Materials in a Selective Detection of Lead(II) from Aqueous Solutions: An Electrochemical Study. *Metals* **2017**, *7*, 124. [CrossRef]
2. Yu, T.; Jiang, T.Y.; Liu, X.; Ma, X.D.; Yang, Z.F.; Hou, Q.Y.; Xia, X.Q.; Li, F.Y. Research progress in current status of soil heavy metal pollution and analysis technology. *Geol. China* **2021**, *48*, 460–476.
3. Boskabady, M.; Marefati, N.; Farkhondeh, T.; Shakeri, F.; Farshbaf, A.; Boskabady, M.H. The effect of environmental lead exposure on human health and the contribution of inflammatory mechanisms, a review. *Environ. Int.* **2018**, *120*, 404–420. [CrossRef] [PubMed]
4. Du, C.; Liu, B.; Hu, J.; Li, H.L. Determination of iodine number of activated carbon by the method of ultraviolet–visible spectroscopy. *Mater. Lett.* **2021**, *285*, 129137. [CrossRef]
5. Viktorija, T.; Jaunius, U.; Dalius, R. A direct electron transfer formaldehyde dehydrogenase biosensor for the determination of formaldehyde in river water. *Talanta* **2021**, *234*, 122657.
6. Zhao, K.; Ge, L.Y.; Wong, T.I.; Zhou, X.D.; Grzegorz, L. Gold-silver nanoparticles modified electrochemical sensor array for simultaneous determination of chromium(III)and chromium(VI)in wastewater samples. *Chemosphere* **2021**, *281*, 130880. [CrossRef] [PubMed]
7. Li, X.; Zou, N.; Wang, Z.X.; Shangguan, W.; Ma, Z.H.; Wang, X.L. Stripping voltammetry detection of Pb2+ using poly(amino benzenesulfonic acid)-MoS2 nanosheets composite membrane modified glassy carbon electrode. *Chin. J. Anal. Lab.* **2020**, *39*, 1075–1079.
8. Hernandez, P.R.; Galan, C.A.; Morales, A.; Alegret, S. Measuring system for amperometric chemical sensors using the three-electrode technique for field application. *J. Appl. Res. Eng. Technol.* **2003**, *1*, 107–113. [CrossRef]
9. Yin, H.S.; Zhou, Y.L.; Ma, Q.; Ai, S.Y.; Chen, Q.P.; Zhu, L.S. Electrocatalytic oxidation behavior of guanosine at graphene, chitosan and Fe_3O_4 nanoparticles modified glassy carbon electrode and its determination. *Talanta* **2010**, *82*, 1193–1199. [CrossRef]
10. Yoshii, T.; Nishitsugu, F.; Kikawada, K.; Maehashi, K.; Ikuta, T. Identification of Cadmium Compounds in a Solution Using Graphene-Based Sensor Array. *Sensors* **2023**, *23*, 1519. [CrossRef]
11. Liu, Q.; Chen, J.; Li, Y.R.; Shi, G.Q. High-performance strain sensors with fish-scale-like graphene-sensing layers for full-range detection of human motions. *ACS Nano* **2016**, *10*, 7901–7906. [CrossRef] [PubMed]
12. Chen, S.; Jiang, K.; Lou, Z.; Chen, D.; Shen, G.Z. Recent developments in graphene-based tactile sensors and E-skins. *Adv. Mater. Technol.* **2018**, *3*, 1700248. [CrossRef]
13. Castro Neto, A.H.; Guinea, F.; Peres, N.M.R.; Novoselov, K.S.; Geim, A.K. The electronic properties of graphene. *Rev. Mod. Phys.* **2009**, *81*, 109–162. [CrossRef]
14. You, R.; Liu, Y.Q.; Hao, Y.L.; Han, D.D.; Zhang, Y.L.; You, Z. Laser Fabrication of Graphene-Based Flexible Electronics. *Adv. Mater.* **2020**, *32*, 1901981. [CrossRef] [PubMed]

15. Qian, Z.S.; Shan, X.Y.; Chai, L.J.; Chen, J.R.; Feng, H. A fluorescent nanosensor based on graphene quantum dots–aptamer probe and graphene oxide platform for detection of lead (II) ion. *Biosens. Bioelectron.* **2015**, *68*, 225–231. [CrossRef]
16. Ullah, S.; Hasan, M.; Ta, H.Q.; Zhao, L.; Shi, Q.; Fu, L.; Choi, J.; Yang, R.Z.; Liu, Z.F.; Rümmeli, M.H. Synthesis of doped porous 3D graphene structures by chemical vapor deposition and its applications. *Adv. Funct. Mater.* **2019**, *29*, 1904457. [CrossRef]
17. Yang, Z.F.; Tian, J.R.; Yin, Z.F.; Cui, C.J.; Qian, W.Z.; Wei, F. Carbon nanotube and graphene-based nanomaterials and applications in high-voltage supercapacitor: A review. *Carbon* **2019**, *141*, 467–480. [CrossRef]
18. Cui, Y.X. Research on Flexible Mechanical Sensor Based on Laser-Induced Graphene. Master's Thesis, Nanjing University of Posts and Telecommunications, Nanjing, China, 2021.
19. Lin, J.; Peng, Z.; Liu, Y.; Francisco, R.Z.; Ye, R.; Samuel, E.L.G.; Yacaman, M.J.; Yakobson, B.Y.; Tour, J.M. Laser-induced porous graphene films from commercial polymers. *Nat. Commun.* **2014**, *5*, 5714. [CrossRef]
20. Ye, R.Q.; James, D.K.; Tour, J.M. Laser-Induced Graphene:From Discovery to Translation. *Adv. Mater.* **2019**, *31*, 1803621. [CrossRef]
21. Lin, K.C.; Muthukumar, S.; Prasad, S. Flex-GO (Flexible graphene oxide) sensor for electrochemical monitoring lactate in low-volume passive perspired human sweat. *Talanta* **2020**, *214*, 120810. [CrossRef]
22. Feng, X.M.; Zhang, Y.; Zhou, J.H.; Li, Y.; Chen, S.F.; Zhang, L.; Ma, Y.W.; Wang, L.H.; Yan, X.H. Three-dimensional nitrogen-doped graphene as an ultrasensitive electrochemical sensor for the detection of dopamine. *Nanoscale* **2015**, *7*, 2427–2432. [CrossRef] [PubMed]
23. Kwak, Y.H.; Choi, D.S.; Kim, Y.N.; Kim, H.; Yoon, D.H.; Ahn, S.S.; Yang, J.W.; Yang, W.S.; Seo, S. Flexible glucose sensor using CVD-grown graphene-based field effect transistor. *Biosens. Bioelectron.* **2012**, *37*, 82–87. [CrossRef] [PubMed]
24. Ruecha, N.; Rodthongkum, N.; Cate, D.M.; Volckens, J.; Chailapakul, O.; Henry, C.S. Sensitive electrochemical sensor using a graphene–polyaniline nanocomposite for simultaneous detection of Zn(II), Cd(II), and Pb(II). *Anal. Chim. Acta* **2015**, *874*, 40–48. [CrossRef]
25. Huang, L.B.; Guo, W.H.; Cheng, L.; Su, J.J.; Song, Y.; Hu, F.J.; Law, Y.L.; Yan, Z.; Lin, J.; Ye, R.Q. Differentiating structure of in situ and ex situ formation of laser-induced graphene hybrids. *Rare Met.* **2022**, *41*, 3035–3044. [CrossRef]
26. Zhang, J.B.; Ren, M.Q.; Li, Y.L.; Tour, J.M. In Situ Synthesis of Efficient Water Oxidation Catalysts in Laser-Induced Graphene. *ACS Energy Lett.* **2018**, *3*, 677–683. [CrossRef]
27. Fu, X.Q.; Duan, S.L.; Lin, J.R.; Shen, M.Q.; Wang, Q.Q. Effects of CeO_2 Nano-Rare Earth Particles Doping on Properties of Ni-Fe-Co-P Alloy Coatings. *Rare Met. Mater. Eng.* **2020**, *49*, 2095–2103.
28. Ren, A.H.; Fu, X.Q.; Duan, S.L.; Shen, M.Q.; Lin, J.R. Effect of Current Density on the Performance of Ni-Fe-P-CeO_2 Composite Coating Prepared by Jet Electrodeposition. *Int. J. Electrochem. Sci.* **2020**, *15*, 8563–8583.
29. Fu, X.Q.; Ma, W.K.; Duan, S.L.; Wang, Q.Q.; Lin, J.R. Electrochemical Corrosion Behavior of Ni-Fe-Co-P Alloy Coating Containing Nano-CeO_2 Particles in NaCl Solution. *Materials* **2019**, *12*, 2614. [CrossRef]
30. Fu, X.Q.; Li, J.; Zhang, H.W.; Xian, J.Y. Simulation and experimental research on nickel-based coating prepared by jet electrodeposition at different scanning speeds. *Int. J. Adv. Manuf. Technol.* **2022**, *121*, 1851–1866. [CrossRef]
31. Duan, S.L.; Fu, X.Q.; Shen, M.Q.; Wang, Q.Q.; Ma, W.K. Study on the corrosion resistance of Ni-P-ZrO_2 composite coating deposited by spray electrodeposition on the surface of rotating body. *Mater. Sci. Technol.* **2020**, *28*, 73–81.
32. Ren, A.H.; Fu, X.Q.; Chen, X.X.; Lin, J.R.; Cao, H.B. Effect of Current Density on the Properties of Ni-CeO_2 Composite Coatings prepared using Magnetic Field-Assisted Jet Electrodeposition. *Int. J. Electrochem. Sci.* **2021**, *16*, 210658.
33. Zhuo, K.; Li, D.; Wang, J.H. TiO_2 Nanotubes/Au Nanoparticles Composites for Electrochemical Sensor of Heavy Metal Ions. *Micronanoelectronic Technol.* **2021**, *58*, 137–143.
34. Liu, Z.G.; Chen, X.; Liu, J.H.; Huang, X.J. Well-arranged porous Co_3O_4 microsheets for electrochemistry of Pb(II) revealed by stripping voltammetry. *Electrochem. Commun.* **2013**, *30*, 59–62. [CrossRef]
35. Armstrong, K.C.; Tatum, C.E.; Dansby-Sparks, R.N. Individual and simultaneous determination of lead, cadmium, and zinc by anodic stripping voltammetry at a bismuth bulk electrode. *Talanta* **2010**, *82*, 675–680. [CrossRef]
36. Tang, S.R.; Ting, T.; You, X.H.; Lu, W.; Chen, J.H.; Li, G.W.; Zhang, L. Label free electrochemical sensor for Pb2+ based on graphene oxide mediated deposition of silver nanoparticles. *Electrochim. Acta* **2016**, *187*, 286–292. [CrossRef]
37. Jeong, S.Y.; MA, Y.W.; Lee, J.U.; Je, G.J.; Shin, B.S. Flexible and Highly Sensitive Strain Sensor Based on Laser-Induced Graphene Pattern Fabricated by 355 nm Pulsed Laser. *Sensors* **2019**, *19*, 4867. [CrossRef] [PubMed]
38. Ferrari, A.C.; Basko, D.M. Raman spectroscopy as a versatile tool for studying the properties of graphene. *Nat. Nanotechnol.* **2013**, *8*, 235–246. [CrossRef]
39. Ferrari, A.C.; Meyer, J.C.; Scardaci, V.; Casiraghi, C.; Lazzeri, M.; Mauri, F.; Piscanec, S.; Jiang, D.; Novoselov, K.S.; Roth, S.; et al. Raman spectrum of graphene and graphene layers. *Phys. Rev. Lett.* **2006**, *97*, 187401. [CrossRef] [PubMed]
40. Casiraghi, C.; Hartschuh, A.; Lidorikis, E.; Qian, H.; Harutyunyan, H.; Gokus, T.; Novoselov, K.S.; Ferrari, A.C. Rayleigh Imaging of Graphene and Graphene Layers. *Nano Lett.* **2007**, *7*, 2711–2717. [CrossRef]
41. Wahab, H.; Jain, V.; Tyrrell, A.S.; Seas, M.A.; Kotthoff, L.; Johnson, P.A. Machine-learning-assisted fabrication: Bayesian optimization of laserinduced graphene patterning using in-situ Raman analysis. *Carbon* **2020**, *167*, 609–619. [CrossRef]
42. Mei, Z.F.; Yao, M.T.; Chen, R.S.; Hu, C.G. Sensitive Non-Enzymatic Glucose Electrochemical Sensor Based on Dendrite Copper Modified Laser-Induced Graphene Electrodes. *J. Anal. Sci.* **2021**, *37*, 522–528.

43. Oliver-Tolentino, A.; Vazquez-Samperio, J.; Manzo-Robledo, A.; González-Huerta, R.; Flores-Moreno, J.; Ramírez-Rosales, D.; Guzmán-Vargas, A. An Approach to Understanding the Electrocatalytic Activity Enhancement by Superexchange Interaction Toward OER in Alkaline Media of Ni-Fe LDH. *J. Phys. Chem. C* **2014**, *118*, 22432–22438. [CrossRef]
44. Gao, R.M.; Liu, H.G. Discussion of Concept of Detection Limit-The Definition, the Estimation and the Use of IUPAC and etc. Approaches. *Chin. J. Anal. Chem.* **1993**, *21*, 1232–1236.

Disclaimer/Publisher's Note: The statements, opinions and data contained in all publications are solely those of the individual author(s) and contributor(s) and not of MDPI and/or the editor(s). MDPI and/or the editor(s) disclaim responsibility for any injury to people or property resulting from any ideas, methods, instructions or products referred to in the content.